

# DCFormer: Efficient 3D Vision-Language Modeling with Decomposed Convolution

Gorkem Can Ates<sup>1</sup>, Kuang Gong<sup>2</sup>, and Wei Shao<sup>1,3,\*</sup>

<sup>1</sup>Department of Medicine, University of Florida, Gainesville, FL, 32611, USA

<sup>2</sup>Department of Biomedical Engineering, University of Florida, Gainesville, FL, 32611, USA

<sup>3</sup>Intelligent Clinical Care Center, University of Florida, Gainesville, FL, 32611, USA

\*Corresponding author. E-mail address: weishao@ufl.edu

## ABSTRACT

Vision-language models (VLMs) align visual and textual representations, enabling high-performance zero-shot classification and image-text retrieval in 2D medical imaging. However, extending VLMs to 3D medical imaging remains computationally challenging. Existing 3D VLMs rely on Vision Transformers (ViTs), which are computationally expensive due to self-attention’s quadratic complexity, or 3D convolutions, which demand excessive parameters and FLOPs as kernel size increases. We introduce DCFormer, an efficient 3D medical image encoder that factorizes 3D convolutions into three parallel 1D convolutions along depth, height, and width. This design preserves spatial information while significantly reducing computational cost. Integrated into a CLIP-based vision-language framework, DCFormer is evaluated on CT-RATE, a dataset of 50,188 paired 3D chest CT volumes and radiology reports, for zero-shot multi-abnormality detection across 18 pathologies. Compared to ViT, ConvNeXt, PoolFormer, and TransUNet, DCFormer achieves superior efficiency and accuracy, with DCFormer-Tiny reaching 62.0% accuracy and a 46.3% F1-score while using significantly fewer parameters. These results highlight DCFormer’s potential for scalable, clinically deployable 3D medical VLMs. Our codes will be publicly available.

## Introduction

Deep learning has revolutionized medical imaging, enabling automated disease diagnosis, accurate prognosis, and personalized treatment planning<sup>1-4</sup>. With the emergence of Convolutional Neural Networks (CNNs)<sup>5,6</sup> and Vision Transformers (ViTs)<sup>7</sup>, deep learning has achieved state-of-the-art performance in supervised tasks such as lesion detection and organ segmentation<sup>8-12</sup>. Despite these advancements, supervised models require training on large-scale manually annotated datasets and lack generalization across diverse medical imaging tasks and modalities.

To mitigate the reliance on labeled data, self-supervised learning (SSL) methods such as masked autoencoders<sup>13</sup> have emerged as powerful techniques for extracting meaningful representations from unlabeled images<sup>14,15</sup>. Despite their advantages, these methods still require supervised fine-tuning on small labeled datasets. Vision-language models (VLMs) such as CLIP (Contrastive Language-Image Pretraining)<sup>16</sup> offer a promising alternative by aligning visual and textual representations in a shared latent space, enabling zero-shot capabilities. Initially successful in natural image domains<sup>17,18</sup>, CLIP has since been adapted for various 2D medical imaging tasks, including zero-shot classification, prompt-driven segmentation, image-text retrieval, radiology report generation, and visual question answering<sup>19-25</sup>.

While CLIP-based approaches have advanced 2D medical imaging, their application to 3D imaging remains underexplored due to several key challenges. A major challenge is the scarcity of large-scale, open-source datasets containing 3D image volumes paired with textual reports. To address this, Hamamci et al.<sup>26</sup> introduced CT-RATE, a dataset consisting of 50,188 reconstructed 3D chest computed tomography (CT) volumes from 25,692 scans of 21,304 patients, along with their corresponding radiology reports. They also proposed CT-CLIP, a 3D VLM for chest CT that employs CT-ViT<sup>27</sup>, a model incorporating a two-stage spatial and temporal transformer. While CT-CLIP performs well in zero-shot detection and image-text retrieval tasks, its use of self-attention mechanisms leads to significant computational overhead. Additionally, its image encoder follows a ViT-like patching strategy, directly downsampling images with a fixed patch size of 20. This strategy leads to feature loss, as it fails to extract hierarchical representations—an essential aspect of medical imaging. Prior studies have shown that hierarchical feature extraction is crucial for capturing spatial and contextual information in medical images<sup>9,10,28</sup>. Despite these limitations, CT-CLIP marks a significant step toward adapting foundation models for 3D medical imaging.

Another challenge is the computational complexity of adapting CLIP-like VLMs to 3D imaging modalities such as CT and magnetic resonance imaging (MRI). The high-resolution, volumetric nature of 3D medical data imposes substantial computational demands, particularly with standard ViT-based or 3D CNN-based encoders. While ViTs effectively capture global spatial relationships, their computational complexity scales quadratically with input size, making them inefficient for 3D

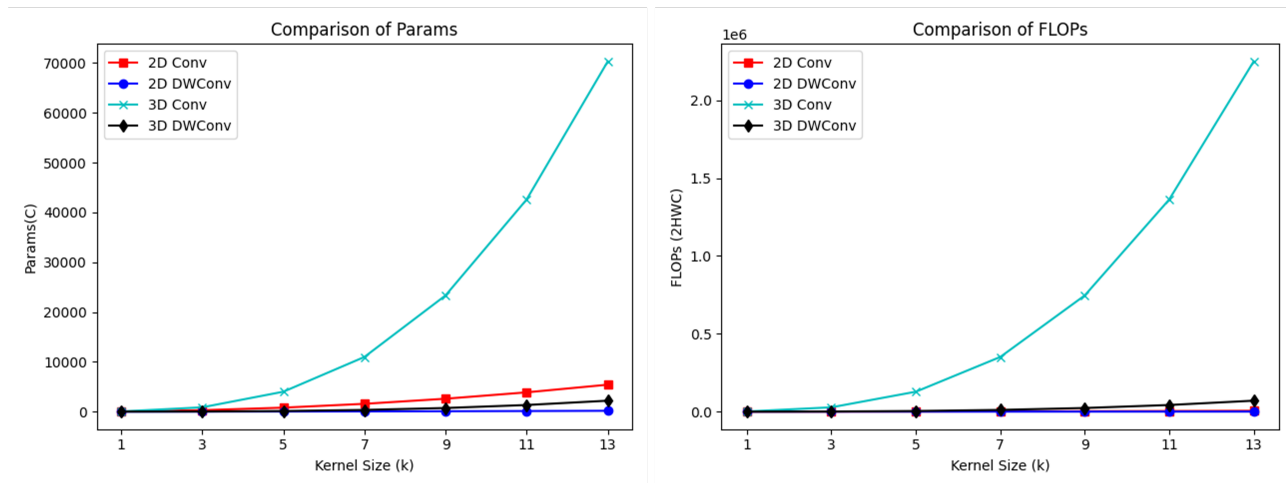


**Figure 1.** FLOP and parameter comparison of 2D and 3D convolutions. For simplicity, we set the number of output channels  $C = 32$  and depth dimension  $D = 32$

volumes. Likewise, 3D convolutions, which are well-suited for capturing local spatial features, become prohibitively expensive with large kernel sizes ( $k > 3$ ). To mitigate this, depthwise convolutions<sup>29</sup> have been explored as an alternative, reducing both parameter count and computational cost. However, they can still be inefficient for 3D imaging when large kernels and high output channel dimensions are required. Figure 1 compares the parameters and FLOPs of 2D and 3D standard versus depthwise convolutions, showing that standard 3D convolutions demand significantly more resources than their 2D counterparts. Although depthwise convolutions improve efficiency, their computational cost scales cubically with kernel size, posing challenges for large 3D medical datasets where large receptive fields are needed to capture complex anatomical structures. Additionally, their cumulative use throughout the network significantly increases the overall computational burden.

To overcome these challenges of existing 3D VLMs, we propose DCFormer, a family of architectures designed for 3D medical imaging. DCFormer introduces decomposed convolutions as an alternative to self-attention and conventional 3D convolutions, significantly reducing computational complexity while preserving the ability to extract both local and global spatial features. By factorizing 3D convolutions into three 1D convolutions along each spatial dimension, DCFormer aims to balance efficiency and performance, significantly reducing model parameters and FLOPs (Figure 2). We integrate DCFormer into the CLIP framework, enabling efficient joint vision-language learning for 3D medical imaging. Our experiments demonstrate that DCFormer achieves competitive zero-shot performance on CT-RATE dataset while significantly reducing computational costs compared to existing state-of-the-art methods. We anticipate that DCFormer will serve as a stepping stone for advancing scalable and efficient image encoders for vision-language understanding and inspire further research into lightweight, high-performance architectures for clinical applications.

## Results

We train a CLIP-based joint vision-language learning framework (see Developing a CLIP framework using DCFormer in the Methods section) using the CT-RATE dataset, consisting of 50,188 non-contrast 3D chest CT volumes paired with corresponding radiology text reports. For the text encoder, we use CXR-BERT<sup>30</sup>. For the image encoder, we comprehensively evaluate our proposed DCFormer architecture by benchmarking its zero-shot performance against several state-of-the-art models, including ViT<sup>7</sup>, CT-ViT<sup>26,27</sup>, TransUNet<sup>9</sup>, ConvNeXt<sup>31</sup>, InceptionNeXt<sup>32</sup>, and PoolFormer<sup>33</sup> (see SOTA image encoders in the Methods section).

### Zero-shot multi-abnormality detection results

Once trained to maximize the similarity between image and text embeddings, the CLIP framework enables multi-abnormality detection by inputting each abnormality as a text prompt (see \*Zero-shot multi-abnormality detection with DCFormer\* in the Methods section). Specifically, we use the prompts "Abnormality is present." and "Abnormality is not present." for each of the 18 distinct abnormalities, following the ablation study by Hamamci et al.<sup>26</sup>. We then compute the normalized probability of each abnormality being present in the CT image and evaluate model performance using accuracy, F1 score, precision, and recall.

Table 1 compares the zero-shot performance and computational efficiency of multiple models on the CT-RATE dataset for

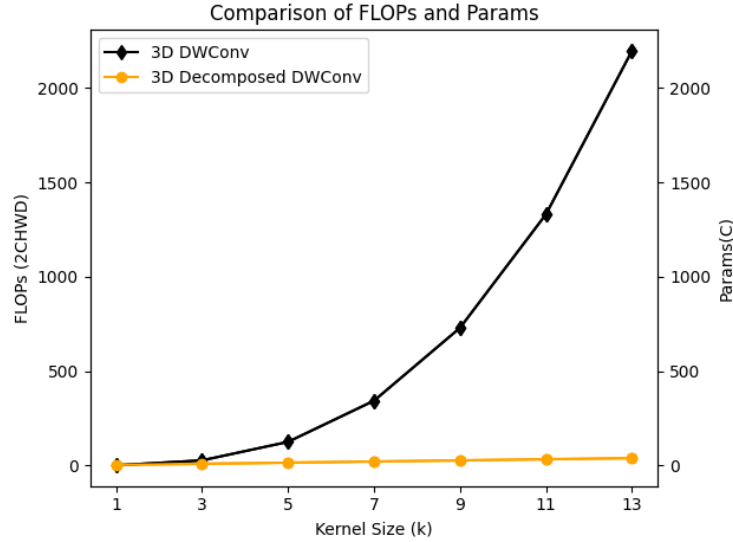


**Figure 2.** FLOP and parameter comparison between 3D depthwise convolution and decomposed depthwise convolution.

model	variant	params (M)	GFLOPs	accuracy (%)	f1 score (%)	precision (%)	recall (%)
DCFormer	nano	920.3K	34.21	60.4	41.9	27.2	62.8
convnext <sup>31</sup>	nano	3.19M	31.92	62.2	39.4	26.7	55.1
poolformer <sup>33</sup>	nano	2.79M	27.14	60.2	37.0	24.8	52.3
DCFormer	naïve	5.85M	49.48	63.1	44.5	29.5	65.5
vit <sup>7</sup>	naïve	11.10M	39.05	55	42.5	25.8	71.5
convnext <sup>31</sup>	naïve	15.63M	96.84	60.7	42.4	27.7	63.8
poolformer <sup>33</sup>	naïve	11.31M	63.75	60.1	39.1	25.7	56.8
transunet <sup>9</sup>	naïve	12.48M	118.9	58.6	41.4	26.5	56.0
DCFormer	tiny	15.1M	168.2	62.0	46.3	29.7	70.1
vit <sup>7</sup>	tiny	26.34M	86.43	61	43.2	28.0	64.8
convnext <sup>31</sup>	tiny	31.59M	156.31	62.5	42.1	28.2	60.1
transunet <sup>9</sup>	tiny	23.93M	207.5	61.5	35.8	24.7	48.7
poolformer <sup>33</sup>	tiny	20.68M	117.46	61.8	38.3	26.0	53.5
ctvit <sup>26</sup>	-	101.1M	160.5	62.9	44.3	29.3	65.7

**Table 1.** Zero-shot performance of models trained on CT-RATE dataset at the resolution of 512x512x256.

image volumes of size 512×512×256. DCFormer provides a family of models with configurations ranging from nano to tiny variants, with parameter counts between 920.3K and 15.1M and GFLOPs spanning 34.21G to 168.2G. As shown in Table 1, DCFormer consistently achieves superior accuracy, F1 score, precision, and recall across all configurations while maintaining computational efficiency.

For instance, the nano variant achieves higher F1 score, precision, and recall than ConvNeXt and PoolFormer, despite having fewer parameters and similar FLOPs. Similarly, the naïve variant outperforms ConvNeXt, PoolFormer, and TransUNet, demonstrating the efficiency and effectiveness of DCFormer’s architecture. Notably, DCFormer achieves these results with substantially fewer computational resources compared to models like TransUNet and CTViT, which require much larger parameter counts and FLOPs. For example, the naïve variant of DCFormer delivers 63.1% accuracy, 44.5% F1 score, 29.5% precision, and 65.5% recall using just 5.85M parameters and 49.48 GFLOPs—far fewer parameters and similar FLOPs compared to CTViT’s 101.1M parameters and 160.5 GFLOPs and TransUNet’s 23.93M parameters and 207.5 GFLOPs.

This efficiency enables DCFormer to achieve robust performance with a simple yet effective architecture, demonstrating its scalability and suitability for applications requiring both high accuracy and computational efficiency. Overall, for zero-shot implementation, DCFormer outperforms other models in efficiency, with its lightweight variants achieving competitive results while significantly reducing computational overhead. DCFormer’s ability to outperform SOTA models with fewer parameters and FLOPs highlights its potential for applications requiring both high performance and computational efficiency.

## Discussion

In this paper, we introduce DCFormer, a novel vision encoder designed to efficiently process 3D medical images within a CLIP-based vision-language framework. DCFormer addresses key computational challenges in 3D CT analysis, where existing models struggle with high-resolution volumetric data due to the quadratic scaling of self-attention in vision transformers and the high computational cost of 3D convolutions. To mitigate these issues, DCFormer leverages decomposed 3D convolutions as a token mixer, reducing FLOPs and parameter count while preserving strong spatial feature extraction capabilities. This design enables superior performance in zero-shot predictions.

We evaluate DCFormer on CT-RATE, a large-scale dataset containing 50,188 reconstructed 3D chest CT volumes paired with radiology reports. The model is tested under the zero-shot setting, benchmarking its performance against state-of-the-art methods including ViT, ConvNeXt, PoolFormer, and TransUNet. Our primary objective is to develop a model with strong zero-shot capabilities for multi-abnormality detection, minimizing the need for task-specific fine-tuning. As shown in Table 1, DCFormer consistently outperforms competing models in accuracy, F1 score, precision, and recall, all while requiring significantly fewer parameters and computational resources. This efficiency is driven by decomposed convolutions, which factorize 3D convolutions into multiple 1D operations along each spatial dimension, striking an optimal balance between performance and efficiency. Unlike CT-ViT and other computationally intensive 3D models, DCFormer offers a lightweight and scalable solution for large-scale 3D medical imaging, making it particularly well-suited for clinical applications requiring real-time decision-making.

While DCFormer demonstrates promising results, several future directions could enhance its capabilities. First, advanced prompt engineering may further improve zero-shot performance by better aligning image-text embeddings for classification tasks. Second, incorporating larger and more diverse datasets across different medical imaging modalities—such as MRI and PET—could improve generalization and further validate DCFormer’s effectiveness. Finally, integrating DCFormer with other VLMs, such as LLaVA<sup>34</sup> and LISA<sup>35</sup>, could expand its applications to visual question answering and prompt-driven 3D image segmentation.

## Methods

Processing 3D CT images presents significant computational challenges due to their high resolution and volumetric complexity. 3D convolution is computationally expensive due to its cubic scaling with kernel size, and the self-attention mechanism further amplifies the burden by scaling quadratically with input size. To address these challenges, we propose DCFormer, a hybrid architecture that decomposes 3D convolution into multiple 1D components, significantly reducing computational overhead. DCFormer adopts MetaFormer<sup>33,36</sup> as its backbone and employs decomposed convolutions as the token mixer for feature extraction. Its hierarchical structure further enhances feature representation in 3D CT images. Finally, the DCFormer-based image encoder is integrated into a CLIP framework for image-text alignment. As demonstrated in our results, this decomposition strategy substantially reduces parameter count and computational cost while maintaining high performance in both zero-shot and fine-tuning settings.

### Formulation of DCFormer block

The core concept, *MetaFormer*<sup>33,36</sup>, is a general architecture abstracted from transformers<sup>37</sup>. In the Metaformer architecture, the token mixer (e.g. self-attention, depthwise convolution) is not specified, while normalization, a channel mixer (e.g. MLP), and residual connections<sup>38</sup> are retained. The input  $I$  is first passed into a patch embedding block, such as a convolution:

$$X = \text{PatchEmbed}(I) = \text{Flatten}(\text{Conv}_{C_0 \rightarrow C}^{(k,s,p)}(I)) \quad (1)$$

where  $X \in \mathbb{R}^{N \times C}$  denotes the embedded tokens with sequence length  $N$  and embedding dimension  $C$ . Here,  $C_0, k, s$  and  $p$  represent input image channels, kernel size, stride and padding, respectively. These embedded tokens are then fed into the Metaformer architecture:

$$X' = X + \text{TokenMixer}(\text{Norm}_1(X)), \quad (2)$$

$$X'' = X' + \sigma(\text{Norm}_2(X')W_1)W_2. \quad (3)$$

Here,  $\text{Norm}_1$  and  $\text{Norm}_2$  are typically batch normalization<sup>39</sup> or layer normalization<sup>40</sup>. The *TokenMixer* serves as the core module for spatial information interaction,  $W_1$  and  $W_2$  are learnable weights in a two-layer channel MLP, and  $\sigma$  is a non-linear activation<sup>41,42</sup>.

To further enhance the MetaFormer architecture, we introduce Decomposed Convolution as the token mixer within the DCFormer block. This design leverages the computational efficiency of decomposed 1D convolutional operations along each spatial axis (height, width, and depth). By splitting the 3D convolution into three parallel 1D convolutions, Decomposed

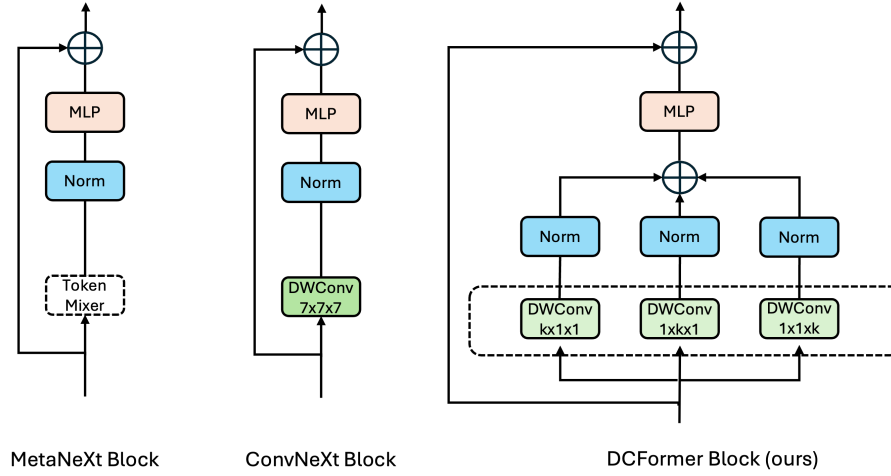


**Figure 3.** Block illustration of MetaNeXt, ConvNeXt and DCFormer.

Convolution captures spatial features while significantly reducing the number of parameters and computational cost. Thus, the DCFormer block integrates decomposed convolutions as a lightweight yet powerful token mixer. Let  $X \in \mathbb{R}^{B \times C \times H \times W \times D}$  denote the input feature map, where  $B$  is the batch size,  $C$  is the number of channels, and  $H$ ,  $W$ , and  $D$  represent the spatial dimensions (height, width, and depth), respectively. The decomposed convolution consists of three 1D depthwise convolutions, processing the input tensor along each spatial axis:

$$X_h^* = \text{DWConv}_{C \rightarrow C}^{k_h \times 1 \times 1}(X), \quad (4)$$

$$X_w^* = \text{DWConv}_{C \rightarrow C}^{1 \times k_w \times 1}(X), \quad (5)$$

$$X_d^* = \text{DWConv}_{C \rightarrow C}^{1 \times 1 \times k_d}(X) \quad (6)$$

where  $(k_h, k_w, k_d)$  represents the kernel sizes in height, width and depth dimensions, respectively. In our implementation, we set  $k_h = k_w = k_d = k \in \{13, 11, 9, 7\}$  to leverage large kernels while maintaining computational efficiency through decomposition. After applying decomposed convolutions along each spatial axis, we normalize the resulting features separately and then combine them using elementwise summation to form the DCFormer block:

$$X' = X + \text{Norm}_h(X_h^*) + \text{Norm}_w(X_w^*) + \text{Norm}_d(X_d^*) \quad (7)$$

An illustration of the DCFormer and its Pytorch-like implementation are shown in Figure 3 and Algorithm 1, respectively.

### Complexity analysis

Given an input tensor  $X \in \mathbb{R}^{1 \times C \times H \times W \times D}$  with batch size  $B = 1$  a 3D depthwise convolution<sup>29</sup> with a kernel size  $(k_h, k_w, k_d)$  where  $k_h = k_w = k_d = k$ , the total parameter count and FLOPs can be calculated as  $Ck^3$  and  $2CHWDk^3$ , respectively (bias is omitted for simplicity). Note that both parameters and FLOPs increase cubically as  $k$  increases. This introduces extensive computational burden, especially for large kernel sizes and when these convolutions are used repeatedly in an end-to-end network, where the effect of the cubic scaling compounds over multiple layers.

By decomposing the 3D depthwise convolution into three 1D depthwise convolutions, the parameter count and FLOPs are significantly reduced to  $3Ck$  and  $6CHWDk$ , respectively, as each 1D convolution operates independently along a single spatial dimension rather than all three simultaneously. A comparison of FLOPs and parameter counts for 3D depthwise and decomposed convolutions is shown in Figure 2. For the decomposed convolution, the computational cost scales linearly with respect to kernel size  $k$ , as opposed to the cubic scaling in the 3D depthwise convolution.

When the kernel size is larger than 3, the complexity increase becomes much more significant. Large kernel sizes such as 7, 11<sup>31,32</sup> and even up to 51<sup>43,44</sup> have been shown to improve model performance. In 3D imaging, our decomposition approach becomes crucial, particularly in deep networks where multiple convolution layers are applied.

### Building a vision encoder with DCFormer

Based on the above findings, we formulate DCFormer as the token mixer and develop a family of architectures of varying sizes, using DCFormer as the main building block. Figure 4 illustrates the general architecture of our proposed DCFormer. Following previous work<sup>31–33,38,45,46</sup>, DCFormer adopts a hierarchical structure with four stages and an initial stem stage following<sup>46,47</sup>.

---

**Algorithm 1:** PyTorch-style pseudocode for DecompConv3D

---

```
class DecompConv3D(nn.Module):
    def __init__(self, dim, kernel_size, stride=1, norm=True, act=None):
        super().__init__()
        # Initialize final activation layer
        self.act = act
        # Initialize normalization layer
        self.norm = nn.ModuleList([nn.BatchNorm3d(dim) if norm else nn.Identity()
            for _ in range(3)])
        # Initialize decomposed convolution layers
        self.c1 = nn.Sequential(
            nn.Conv3d(dim, dim, kernel_size=(kernel_size, 1, 1),
                padding=(kernel_size//2, 0, 0), stride=stride, groups=dim),
            self.norm[0])
        self.c2 = nn.Sequential(
            nn.Conv3d(dim, dim, kernel_size=(1, kernel_size, 1),
                padding=(0, kernel_size//2, 0), stride=stride, groups=dim),
            self.norm[1])
        self.c3 = nn.Sequential(
            nn.Conv3d(dim, dim, kernel_size=(1, 1, kernel_size),
                padding=(0, 0, kernel_size//2), stride=stride, groups=dim),
            self.norm[2])
    def forward(self, x):
        x = self.c1(x) + self.c2(x) + self.c3(x)
        if self.act is not None:
            x = self.act(x)
        return x
```

---

In the stem stage, we use a decomposed convolution with a kernel size of 7 and a stride of 4. The downsampled images are then processed with three additional decomposed convolutions, each with a kernel size of 3 and a stride of 1. The outputs of the stem stage are passed into the hierarchical structure, where each stage produces tokens of sizes  $\frac{H}{8} \times \frac{W}{8} \times \frac{D}{8}$ ,  $\frac{H}{16} \times \frac{W}{16} \times \frac{D}{16}$ ,  $\frac{H}{32} \times \frac{W}{32} \times \frac{D}{32}$ , and  $\frac{H}{64} \times \frac{W}{64} \times \frac{D}{64}$ , respectively, where  $H, W, D$  represent height, width and depth of the input image volume.

We propose four model variants: nano, naive, tiny, small. The number of layers in each stage are [1, 1, 1, 1] for nano, [2, 2, 2, 2] for naive, [2, 3, 3, 2] for tiny and [2, 3, 6, 2] for small models. Additionally, each stage begins with patch embedding where a 3D max pooling operation with a kernel size of 3 and a stride of 2 is used to reduce the image dimensions<sup>47</sup>. Following<sup>7,31,32</sup>, we set the MLP ratio to 4, while the kernel size for the decomposed convolution is set to 7, as in<sup>31,45</sup>. Further configuration details are provided in Table 2.

### Developing a CLIP framework using DCFormer

The CLIP framework aligns visual and contextual embeddings in a shared latent space through contrastive learning (Figure 5(a)). In this paper, we integrate our proposed DCFormer as the vision encoder in CLIP, serving as the primary module for efficient processing of 3D medical images. For the text encoder, we incorporate CXR-BERT<sup>30</sup>, following the implementation in Hamamci et al.<sup>26</sup>. To compute similarities between images and radiology reports, we project visual and textual features into a shared 512-dimensional embedding space. Specifically, we apply global average pooling, followed by a linear projection to the output of the image encoder, while the text encoder output is transformed using a separate linear layer. Finally, visual and textual embeddings are aligned using a contrastive loss function<sup>16</sup>:

$$\mathcal{L}_{\text{CLIP}} = -\frac{1}{B} \sum_{i=1}^B \left[ \log \frac{\exp(\text{sim}(z_i^t, z_i^v)/\tau)}{\sum_{j=1}^B \exp(\text{sim}(z_i^t, z_j^v)/\tau)} + \log \frac{\exp(\text{sim}(z_i^v, z_i^t)/\tau)}{\sum_{j=1}^B \exp(\text{sim}(z_i^v, z_j^t)/\tau)} \right] \quad (8)$$

where  $\text{sim}(z_i^t, z_j^v)$  represents the cosine similarity between the text embedding  $z_i^t$  for the  $i$ -th radiology report and the visual embedding  $z_j^v$  for the  $j$ -th 3D image,  $\tau$  is the temperature parameter (set to 1), and  $B$  is the number of text-image pairs in a training batch.

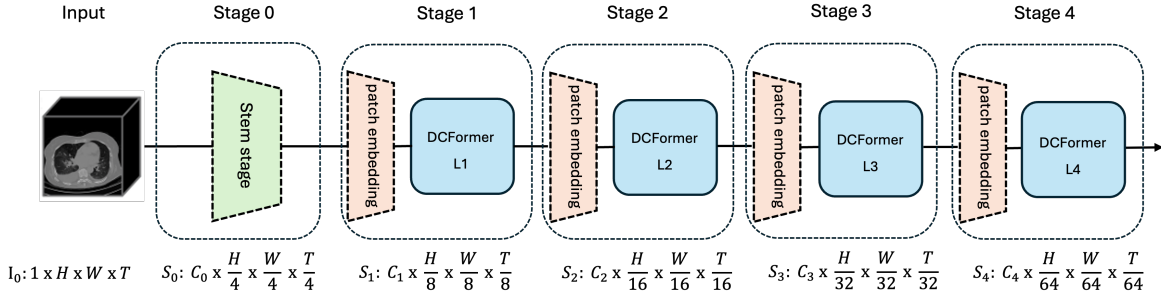


**Figure 4.** Overview of DCFormer

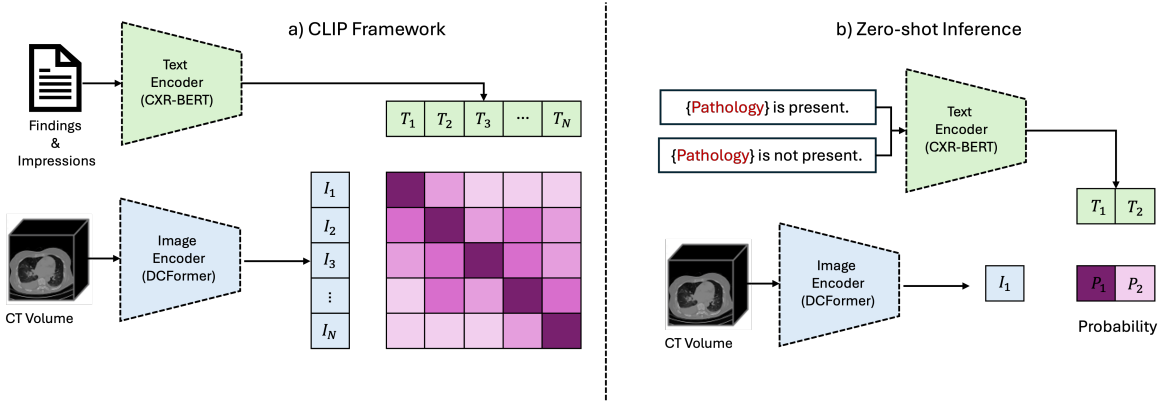


**Figure 5.** CLIP a) training and b) zero-shot inference framework

Unlike CT-CLIP<sup>26</sup>, which lacks explicit multi-scale feature extraction, our DCFormer-based CLIP framework introduces a hierarchical structure that captures multi-scale features across different spatial resolutions. This design enhances representation learning and improves the alignment between image and text embeddings by preserving both global context and fine-grained details—crucial for accurate 3D CT image interpretation. Additionally, integrating DCFormer helps address the computational challenges associated with 3D CT imaging. By utilizing decomposed convolutions, our framework effectively reduces both the parameter count and computational overhead while maintaining robust feature extraction capabilities. As a result, the DCFormer-based CLIP framework is well-suited for large-scale 3D medical imaging applications.

### Zero-shot multi-abnormality detection with DCFormer

For zero-shot multi-abnormality detection, we follow the same approach as CheXzero<sup>21</sup> and CT-CLIP<sup>26</sup>. Specifically, two similarity scores are computed using the cosine similarity between the embedding of the CT image of interest and the embeddings of a positive ('{Pathology} is present.') prompt and a negative ('{Pathology} is not present.') prompt. A softmax function is then applied to these similarity scores to estimate the likelihood of each abnormality being present in the given CT image (see Figure 5 (b) for illustration). It should be noted that the zero-shot performance can potentially be improved by experimenting with different prompt variations. For instance, possible prompt templates including: 'Signs of {Pathology} are/are not detected in the image.', 'There is/is not {Pathology}.', '{Pathology} is/is not observed.' 'Indication/No indication of {Pathology}'. Although prompt engineering plays a critical role in improving image-text alignment, we adopt the prompt structure proposed by Hamamci et al.<sup>26</sup> ('{Pathology} is/is not present.') to maintain consistency with prior work and ensure a fair comparison.

### State-of-the-art image encoders

The pioneering work ViT<sup>7</sup> introduced the concept of processing images as sequences of patches, leveraging the self-attention mechanism for global feature extraction. However, its quadratic complexity imposes a significant computational burden, particularly for 3D medical images. TransUNet<sup>9</sup> was the first model to incorporate ViTs into medical image segmentation, employing a hybrid architecture that combines CNNs with transformers. ConvNeXt<sup>31</sup> demonstrated that 7×7 depthwise convolutions can serve as an effective token mixer, improving performance over self-attention while maintaining computational efficiency. PoolFormer<sup>33</sup> introduced a more efficient feature extraction mechanism than ConvNeXt, replacing self-attention with a simple average pooling operation to minimize computational overhead while preserving strong performance.

Stage	#Tokens	Layer Specification		DCFormer			
				Nano	Naive	Tiny	Small
0	H/4 X W/4 X D/4	STEM	Embed. Dim.	32		64	
			#Blocks	4			
			Patch size (block 1)	7 x 7 x 7, stride 4			
			Patch size (block 2, 3, 4)	3 x 3 x 3, stride 1			
1	H/8 X W/8 X D/8	Patch Embedding	Patch size	3 x 3 x 3, stride 2			
			Embed. Dim.	32	64	96	
		DCFormer Block	Kernel size	7			
			MLP Ratio	4			
			#Blocks	1	2		
2	H/16 X W/16 X D/16	Patch Embedding	Patch size	3 x 3 x 3, stride 2			
			Embed. Dim.	64	128	192	
		DCFormer Block	Kernel size	7			
			MLP Ratio	4			
			#Blocks	1	2	3	
3	H/32 X W/32 X D/32	Patch Embedding	Patch size	3 x 3 x 3, stride 2			
			Embed. Dim.	128	256	384	
		DCFormer Block	Kernel size	7			
			MLP Ratio	4			
			#Blocks	1	2	3	6
4	H/64 X W/64 X D/64	Patch Embedding	Patch size	3 x 3 x 3, stride 2			
			Embed. Dim.	256	512	768	
		DCFormer Block	Kernel size	7			
			MLP Ratio	4			
			#Blocks	1	2		
Parameters (M)				0.92	5.85	15.1	26.86
FLOPS(G)				34.21	49.48	168.2	202.9

**Table 2.** DCFormer configuration details.

### Datasets

For model training and evaluation, we used the open-source CT-RATE dataset<sup>26</sup>, which consists of 50,188 reconstructed CT volumes from 25,692 distinct CT experiments involving 21,304 patients. Each CT volume is paired with a radiology report. The dataset also includes 18 distinct abnormalities extracted from medical reports of each CT scan (findings and impressions). Table 3 provides an in-depth overview of CT-RATE, detailing the distribution of abnormalities across training and validation subsets. Each abnormality is associated with the number of samples in both sets, along with their respective ratios within the dataset. These ratios represent the proportion of samples for each abnormality relative to the total dataset. Notably, the ratios for the training and validation sets remain nearly identical across all abnormalities, ensuring that the validation set accurately reflects the training distribution, making it reliable for evaluating model performance.

### Implementation details

For model training, we follow the same data splitting and pre-processing strategy as in<sup>26</sup>. Specifically, we use 20,000 patients for training and 1,304 for validation. For pre-processing, we first resize each CT volume to a spacing of 0.75 mm on the x-axis and y-axis and 1.5 mm on the z-axis. Then, the volumes are center-cropped or padded to a fixed size of 512 x 512 x 256. Finally, we clip the Hounsfield Unit (HU) values of each CT image volume to [-1000,1000] and normalize them to [-1,1]. We train models using the AdamW optimizer<sup>48</sup> with an initial learning rate  $1^{-5}$ . We do not apply learning rate scheduling or warmup, as we have not observed any significant improvements. All models are trained for 15 epochs.



Abnormality	Number of samples (train)	Number of samples (validation)	Ratio in the dataset (train)	Ratio in the dataset (validation)
Medical Material	5818	313	0.123	0.103
Arterial wall calcification	13377	867	0.284	0.285
Cardiomegaly	5308	325	0.113	0.107
Pericardial effusion	3412	226	0.072	0.074
Coronary artery wall calcification	12025	765	0.255	0.252
Hiatal hernia	6751	417	0.143	0.137
Lymphadenopathy	12221	789	0.259	0.260
Emphysema	9122	600	0.193	0.197
Atelectasis	12263	713	0.260	0.235
Lung nodule	21382	1361	0.453	0.448
Lung opacity	17420	1184	0.369	0.390
Pulmonary fibrotic sequela	12589	831	0.267	0.273
Pleural effusion	5705	376	0.121	0.124
Mosaic attenuation pattern	3638	253	0.077	0.083
Peribronchial thickening	4973	355	0.105	0.117
Consolidation	8319	581	0.176	0.191
Bronchiectasis	4732	330	0.100	0.109
Interlobular septal thickening	3745	249	0.079	0.082

**Table 3.** Detailed overview of the CT-RATE dataset for each abnormality and their distributions in the training and validation sets.<sup>26</sup>

## References

1. Litjens, G. *et al.* A survey on deep learning in medical image analysis. *Med. image analysis* **42**, 60–88 (2017).
2. Esteva, A. *et al.* Deep learning-enabled medical computer vision. *NPJ digital medicine* **4**, 5 (2021).
3. Shen, D., Wu, G. & Suk, H.-I. Deep learning in medical image analysis. *Annu. review biomedical engineering* **19**, 221–248 (2017).
4. Fink, O. *et al.* Potential, challenges and future directions for deep learning in prognostics and health management applications. *Eng. Appl. Artif. Intell.* **92**, 103678 (2020).
5. Fukushima, K. Neocognitron: A self-organizing neural network model for a mechanism of pattern recognition unaffected by shift in position. *Biol. cybernetics* **36**, 193–202 (1980).
6. LeCun, Y. *et al.* Handwritten digit recognition with a back-propagation network. *Adv. neural information processing systems* **2** (1989).
7. Dosovitskiy, A. An image is worth 16x16 words: Transformers for image recognition at scale. *arXiv preprint arXiv:2010.11929* (2020).
8. Ronneberger, O., Fischer, P. & Brox, T. U-net: Convolutional networks for biomedical image segmentation. In *Medical image computing and computer-assisted intervention—MICCAI 2015: 18th international conference, Munich, Germany, October 5–9, 2015, proceedings, part III 18*, 234–241 (Springer, 2015).
9. Chen, J. *et al.* Transunet: Transformers make strong encoders for medical image segmentation. *arXiv preprint arXiv:2102.04306* (2021).
10. Cao, H. *et al.* Swin-unet: Unet-like pure transformer for medical image segmentation. In *European conference on computer vision*, 205–218 (Springer, 2022).
11. Wang, H., Cao, P., Wang, J. & Zaiane, O. R. Uctransnet: rethinking the skip connections in u-net from a channel-wise perspective with transformer. In *Proceedings of the AAAI conference on artificial intelligence*, vol. 36, 2441–2449 (2022).
12. Ates, G. C., Mohan, P. & Celik, E. Dual cross-attention for medical image segmentation. *Eng. Appl. Artif. Intell.* **126**, 107139 (2023).
13. He, K. *et al.* Masked autoencoders are scalable vision learners. In *Proceedings of the IEEE/CVF conference on computer vision and pattern recognition*, 16000–16009 (2022).
14. Tang, Y. *et al.* Self-supervised pre-training of swin transformers for 3d medical image analysis. In *Proceedings of the IEEE/CVF conference on computer vision and pattern recognition*, 20730–20740 (2022).

15. Chen, R. J. *et al.* Scaling vision transformers to gigapixel images via hierarchical self-supervised learning. In *Proceedings of the IEEE/CVF Conference on Computer Vision and Pattern Recognition*, 16144–16155 (2022).
16. Radford, A. *et al.* Learning transferable visual models from natural language supervision. In *International conference on machine learning*, 8748–8763 (PMLR, 2021).
17. Lin, Z. *et al.* Frozen clip models are efficient video learners. In *European Conference on Computer Vision*, 388–404 (Springer, 2022).
18. Thengane, V., Khan, S., Hayat, M. & Khan, F. Clip model is an efficient continual learner. *arXiv preprint arXiv:2210.03114* (2022).
19. Koleilat, T., Asgariandehkordi, H., Rivaz, H. & Xiao, Y. Medclip-samv2: Towards universal text-driven medical image segmentation. *arXiv preprint arXiv:2409.19483* (2024).
20. Lu, M. Y. *et al.* A multimodal generative ai copilot for human pathology. *Nature* **634**, 466–473 (2024).
21. Tiu, E. *et al.* Expert-level detection of pathologies from unannotated chest x-ray images via self-supervised learning. *Nat. Biomed. Eng.* **6**, 1399–1406 (2022).
22. Endo, M., Krishnan, R., Krishna, V., Ng, A. Y. & Rajpurkar, P. Retrieval-based chest x-ray report generation using a pre-trained contrastive language-image model. In *Machine Learning for Health*, 209–219 (PMLR, 2021).
23. Hu, B., Vasu, B. & Hoogs, A. X-mir: Explainable medical image retrieval. In *Proceedings of the IEEE/CVF Winter Conference on Applications of Computer Vision*, 440–450 (2022).
24. Eslami, S., Meinel, C. & De Melo, G. Pubmedclip: How much does clip benefit visual question answering in the medical domain? In *Findings of the Association for Computational Linguistics: EACL 2023*, 1181–1193 (2023).
25. Huang, Z., Bianchi, F., Yuksekogonul, M., Montine, T. J. & Zou, J. A visual–language foundation model for pathology image analysis using medical twitter. *Nat. medicine* **29**, 2307–2316 (2023).
26. Hamamci, I. E. *et al.* A foundation model utilizing chest ct volumes and radiology reports for supervised-level zero-shot detection of abnormalities. *CoRR* (2024).
27. Hamamci, I. E. *et al.* Generatect: Text-conditional generation of 3d chest ct volumes. In *European Conference on Computer Vision*, 126–143 (Springer, 2025).
28. Hatamizadeh, A. *et al.* Swin unetr: Swin transformers for semantic segmentation of brain tumors in mri images. In *International MICCAI brainlesion workshop*, 272–284 (Springer, 2021).
29. Chollet, F. Xception: Deep learning with depthwise separable convolutions. In *Proceedings of the IEEE conference on computer vision and pattern recognition*, 1251–1258 (2017).
30. Boecking, B. *et al.* Making the most of text semantics to improve biomedical vision–language processing. In *European conference on computer vision*, 1–21 (Springer, 2022).
31. Liu, Z. *et al.* A convnet for the 2020s. In *Proceedings of the IEEE/CVF conference on computer vision and pattern recognition*, 11976–11986 (2022).
32. Yu, W., Zhou, P., Yan, S. & Wang, X. Inceptionnext: When inception meets convnext. In *Proceedings of the IEEE/CVF Conference on Computer Vision and Pattern Recognition*, 5672–5683 (2024).
33. Yu, W. *et al.* Metaformer is actually what you need for vision. In *Proceedings of the IEEE/CVF conference on computer vision and pattern recognition*, 10819–10829 (2022).
34. Liu, H., Li, C., Wu, Q. & Lee, Y. J. Visual instruction tuning. *Adv. neural information processing systems* **36** (2024).
35. Lai, X. *et al.* Lisa: Reasoning segmentation via large language model. In *Proceedings of the IEEE/CVF Conference on Computer Vision and Pattern Recognition*, 9579–9589 (2024).
36. Yu, W. *et al.* Metaformer baselines for vision. *IEEE Transactions on Pattern Analysis Mach. Intell.* (2023).
37. Vaswani, A. Attention is all you need. *Adv. Neural Inf. Process. Syst.* (2017).
38. He, K., Zhang, X., Ren, S. & Sun, J. Deep residual learning for image recognition. In *Proceedings of the IEEE conference on computer vision and pattern recognition*, 770–778 (2016).
39. Ioffe, S. Batch normalization: Accelerating deep network training by reducing internal covariate shift. *arXiv preprint arXiv:1502.03167* (2015).
40. Ba, J. L. Layer normalization. *arXiv preprint arXiv:1607.06450* (2016).

41. Nair, V. & Hinton, G. E. Rectified linear units improve restricted boltzmann machines. In *Proceedings of the 27th international conference on machine learning (ICML-10)*, 807–814 (2010).
42. Hendrycks, D. & Gimpel, K. Gaussian error linear units (gelus). *arXiv preprint arXiv:1606.08415* (2016).
43. Ding, X., Zhang, X., Han, J. & Ding, G. Scaling up your kernels to 31x31: Revisiting large kernel design in cnns. In *Proceedings of the IEEE/CVF conference on computer vision and pattern recognition*, 11963–11975 (2022).
44. Liu, S. *et al.* More convnets in the 2020s: Scaling up kernels beyond 51x51 using sparsity. *arXiv preprint arXiv:2207.03620* (2022).
45. Liu, Z. *et al.* Swin transformer: Hierarchical vision transformer using shifted windows. In *Proceedings of the IEEE/CVF international conference on computer vision*, 10012–10022 (2021).
46. Wang, W. *et al.* Internimage: Exploring large-scale vision foundation models with deformable convolutions. In *Proceedings of the IEEE/CVF conference on computer vision and pattern recognition*, 14408–14419 (2023).
47. Dai, Z., Liu, H., Le, Q. V. & Tan, M. Coatnet: Marrying convolution and attention for all data sizes. *Adv. neural information processing systems* **34**, 3965–3977 (2021).
48. Kingma, D. P. Adam: A method for stochastic optimization. *arXiv preprint arXiv:1412.6980* (2014).

## Acknowledgements

This work was supported by the Department of Medicine and the Intelligent Clinical Care Center at the University of Florida College of Medicine.

## Author contributions statement

G.C.A. conducted study design, software development, experimental setup, data analysis, visualization, and manuscript writing. K.G. provided numerous insights and contributed to discussions throughout this study. W.S. oversaw the project, conducted study design, experimental setup, and data analysis, and contributed to manuscript writing. All authors reviewed the manuscript.

## Additional information

**Competing interests** The authors have no conflict of interest to declare.